

What produces the far-infrared/submillimetre emission in the most luminous QSOs?

M. Symeonidis[★]

Mullard Space Science Laboratory, University College London, Holmbury St. Mary, Dorking, Surrey RH5 6NT, UK

Accepted 2016 October 25. Received 2016 October 25; in original form 2016 May 20

ABSTRACT

The AGN.

I examine the average spectral energy distributions (SEDs) of two samples of the most powerful, unobscured quasi-stellar objects (QSOs) at $2 < z < 3.5$, with rest-frame optical luminosities in the range of $46.2 < \log \nu L_\nu (5100 \text{ \AA}) < 47.4$, corresponding to the tail of the $2 < z < 4$ QSO optical luminosity function. I find that the active galactic nucleus (AGN) could potentially account for the entire broad-band emission from the ultraviolet to the submillimetre (submm), on the basis that the SEDs of these sources are similar to the intrinsic AGN SEDs derived for lower power, lower redshift QSOs. Although this does not preclude substantial star formation in their host galaxies, I find that the AGN dominates the total infrared (IR) luminosity, removing the necessity for a star-forming component in the far-IR/submm. I argue that the origin of the far-IR/submm emission in such powerful QSOs includes a small contribution from the AGN torus but is predominantly linked to dust at kpc-scales heated by the AGN. The latter component accounts for at least 5–10 per cent of the bolometric AGN luminosity and has an implied dust mass of the order of $10^8 M_\odot$.

Key words: galaxies: active – quasars: general – infrared: general – submillimetre: general.

1 INTRODUCTION

It is now well established that the most energetic, non-transient sources in the Universe are active galactic nuclei (AGN), the most optically luminous of which are often referred to as quasi-stellar objects (QSOs). The first QSOs were identified via their radio emission (Greenstein & Matthews 1963; Schmidt 1963), but in the last few decades, the number of known luminous and/or high-redshift QSOs has significantly increased, thanks to large-scale optical surveys such as the SDSS (Alam et al. 2015) and 2 dF/6 dF (Colless et al. 2001; Jones et al. 2009), and near-infrared (near-IR) surveys such as 2MASS (Skrutskie et al. 2006) and UKIDSS (Lawrence et al. 2007). The last few years saw the discovery of the most luminous QSO, SDSS J010013.02+280225.8, found at $z = 6.3$ with a bolometric luminosity of $1.62 \times 10^{48} \text{ erg s}^{-1}$ (Wu et al. 2015). Numerous powerful QSOs have been detected outside the local Universe, although their existence at high redshifts (e.g. Willott et al. 2010a,b; De Rosa et al. 2011; Podigachoski et al. 2015) poses challenges in our understanding of supermassive black hole growth in the early Universe (e.g. Volonteri 2012; Melia 2014).

In recent years, much effort has been focused on studying the types of galaxies which powerful AGN reside in (e.g. Mainieri et al. 2011; Khandai et al. 2012; Rawlings et al. 2013; Feruglio et al. 2014; Podigachoski et al. 2015), with the ultimate aim to understand the origin of the black hole–galaxy bulge mass relation

in the nearby Universe (e.g. Magorrian et al. 1998; Ferrarese & Merritt 2000), as well as the reason behind the co-evolution of the star formation rate (SFR) density and AGN accretion rate density (e.g. Boyle & Terlevich 1998; Merloni, Rudnick & Di Matteo 2004; Silverman et al. 2008; Hirschmann et al. 2014). Indeed, AGN hold a central role in models of galaxy formation and evolution, AGN feedback being essential in shaping the high-mass end of the galaxy luminosity function (e.g. Bower et al. 2006; Croton et al. 2006).

Since galaxy evolution is directly linked to the rate of star formation and consumption of gas, as well as any processes, such as AGN feedback, which might interfere with it, one of the key properties of AGN host galaxies to chart is the SFR. For unresolved sources, the AGN and stellar contributions to the global galaxy emission must be disentangled through spectral energy distribution (SED) fitting, a non-trivial task in its own right as it requires a priori knowledge of the strength of either one component over the entire electromagnetic spectrum. In most cases, the host cannot be seen at X-ray to mid-IR wavelengths. For non-Compton-thick AGN, X-ray emission is unequivocally AGN dominated as the X-ray luminosity from stellar processes, even for the most rapidly star forming galaxies, is orders of magnitude lower than that of powerful AGN (e.g. Symeonidis et al. 2011, 2014). The optical spectra and optical broad-band photometry of luminous unobscured QSOs are also AGN dominated, as is the case for the near- and mid-IR, the origin of which is emission from the dusty torus (e.g. Osterbrock & Ferland 2006; Rodriguez-Ardila & Mazzalay 2006). However, it is often assumed that the far-IR and submillimetre (submm) part of the

[★] E-mail: m.symeonidis@ucl.ac.uk

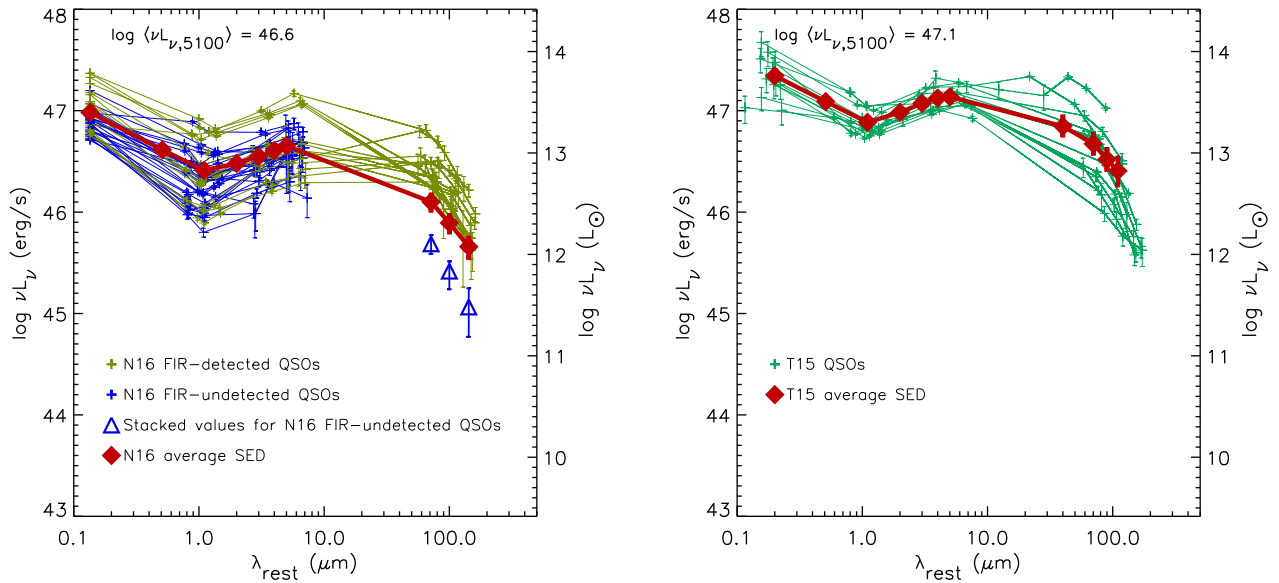


Figure 1. SEDs for the **N16** (left-hand panel) and **T15** (right-hand panel) QSO samples. The red diamonds are the average SED of each sample.

broad-band SED, which in star-forming galaxies is a robust tracer of the SFR (e.g. Kennicutt 1998; Kennicutt & Evans 2012), has but a minor contribution from the AGN and hence directly traces star formation even in AGN hosts. Since the advent of the *Herschel* space observatory, which for the first time provided far-IR/submm data for many high-redshift galaxies hosting powerful AGN, *Herschel* far-IR SPIRE and/or PACS photometry has been frequently used to compute the SFRs of AGN hosts (e.g. Rovilos et al. 2012; Rosario et al. 2013; Drouart et al. 2014; Netzer et al. 2014, 2016; Delvecchio et al. 2015; Mullaney et al. 2015; Tsai et al. 2015).

Recently, in Symeonidis et al. (2016, hereafter S16), we showed that the aforementioned assumptions regarding the AGN contribution to the far-IR/submm are not always valid. We derived an intrinsic AGN SED from the optical to submm, by using mid-IR spectral lines to subtract the host galaxy component in a sample of powerful nearby QSOs, and noted that the intrinsic AGN SED retains a higher level of far-IR/submm power than previously thought. Our results indicated that for some galaxies hosting luminous [$\nu L_{\nu, 5100}$ or $L_{X(2-10\text{keV})} \gtrsim 10^{43.5} \text{ erg s}^{-1}$] AGN, the entire broad-band SED could be AGN dominated at least up to 1000 μm , the far-IR/submm emission being associated with AGN-heated dust at kpc scales.

In this paper, I examine the SEDs of two samples consisting of the most luminous unobscured QSOs at $2 < z < 3.5$ in order to determine the origin of their far-IR/submm emission. The paper is laid out as follows. In Section 2, I describe the samples and SEDs and in Section 3, I report my results. The discussion and conclusions are presented in Section 4. Throughout, I adopt a concordance cosmology of $H_0 = 70 \text{ km s}^{-1} \text{ Mpc}^{-1}$, $\Omega_M = 1 - \Omega_\Lambda = 0.3$.

2 THE SAMPLE

I select two samples consisting of the most powerful, unobscured QSOs which have available mid- and far-IR data, taken from Tsai et al. (2015, hereafter T15) and Netzer et al. (2016, hereafter N16); these QSOs are at $2 < z < 3.5$ and have a rest-frame optical luminosity $\log \nu L_{\nu}(5100 \text{ \AA}) = 46.2\text{--}47.4$. From N16, I chose their most luminous subsample of objects, which they define as $\log \nu L_{\nu}(1350 \text{ \AA}) > 46.7$, consisting of 15 far-IR-detected and 28

far-IR-undetected QSOs. The T15 sample consists of 12 far-IR-detected QSOs, on average about 0.5 dex more luminous in the optical than the N16 sample.

Fig. 1 shows their SEDs; for the N16 far-IR-undetected QSOs, rest-frame stacked luminosities from N16 calculated at a nominal redshift of 2.5 are also plotted. To calculate an average SED for the whole N16 sample, I first compute the average SEDs of the far-IR-detected and far-IR-undetected sources separately. For the former, I logarithmically interpolate between the data points, obtaining rest-frame luminosities at 0.135, 0.51, 1, 2, 3, 4, 5, 71, 100 and 143 μm . The luminosities at each of those wavelengths are subsequently averaged. For the far-IR-undetected sample, I logarithmically interpolate their SEDs up to 5 μm , subsequently computing average rest-frame luminosities at 0.135, 0.51, 1, 2, 3, 4 and 5 μm and combining those with the far-IR-stacked luminosities at 71, 100 and 143 μm in order to get a full average SED for this subgroup. Once I have an average SED for each subgroup, I determine the weighted average SED of the whole N16 sample. To evaluate the errors on the average luminosities up to 5 μm , I combine the standard errors of the average luminosities of each subsample. For the far-IR part of the SED, I combine the errors from stacking for the far-IR-undetected subsample with the standard errors of the far-IR-detected subsample. In both cases, I perform weighted error propagation, i.e. taking into account the number of sources in each subgroup.

To obtain an average SED for the T15 sample (all of which are far-IR detected), I logarithmically interpolate between the data in order to compute rest-frame luminosities at 0.2, 0.51, 1, 2, 3, 4, 5, 40, 70, 90 and 110 μm and subsequently average those. Since I have full SEDs for all sources in the T15 sample, I calculate errors on the average luminosities by bootstrapping. The average SEDs are shown in Fig. 1 as red diamonds. The mean 5100 \AA luminosity of the N16 and T15 samples is $10^{46.6}$ and $10^{47.1} \text{ erg s}^{-1}$, respectively.

3 RESULTS

3.1 SED comparison

To explore the origin of the broad-band emission in these QSOs, I compare the average SED of each QSO sample with the intrinsic

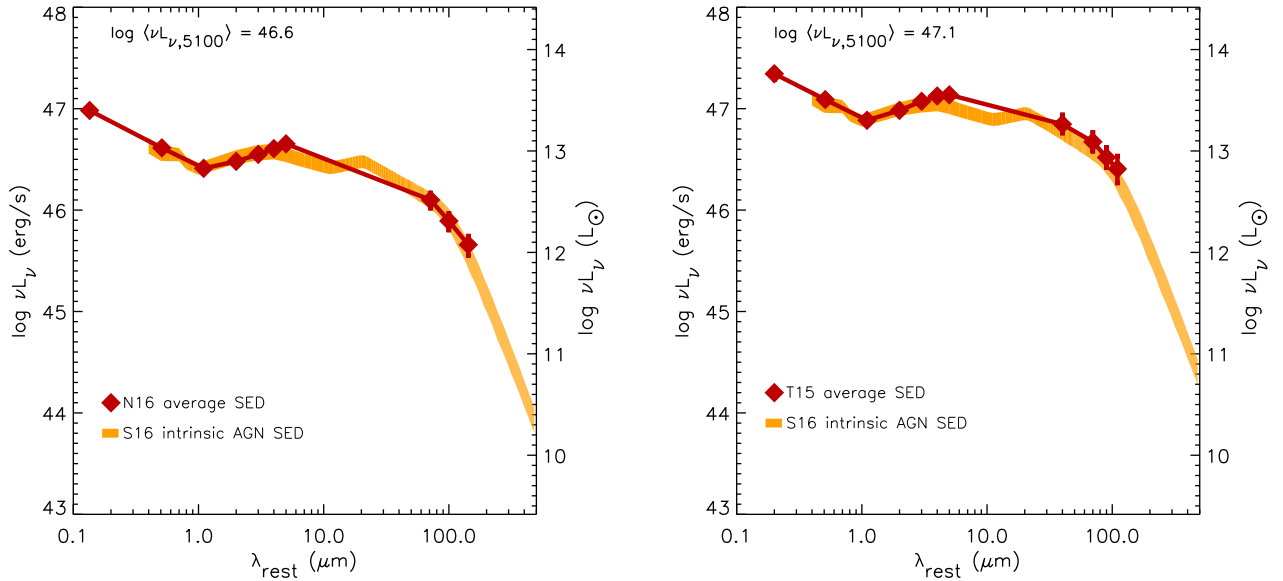


Figure 2. The intrinsic AGN SED from S16 (shaded orange region where the shading width represents the 1σ bounds) normalized at $1\ \mu\text{m}$ to the average SEDs of the two samples (red diamonds).

AGN SED derived in S16, normalizing the latter at a $1\ \mu\text{m}$ rest frame (Fig. 2). The S16 SED is the average, intrinsic, broad-band emission from the AGN in a sample of optically luminous ($L_{5100} > 10^{43.5}\ \text{erg s}^{-1}$), unobscured, radio-quiet, $z < 0.18$, QSOs from the Palomar Green survey. (We refer the reader to S16 for more details.) As the S16 SED is an *average*, it is more appropriate to compare it with the average emission of uniformly selected samples of QSOs, as opposed to individual SEDs. Fig. 2 shows this comparison. I find that the average SEDs of the two QSO samples examined here are not significantly different from the intrinsic AGN SED derived in S16; no data point is more than 1.3σ away from the S16 SED. The maximum difference is at $5\ \mu\text{m}$ where the N16 and T15 average SEDs are 26 and 28 per cent higher than the S16 SED, respectively, suggesting a stronger mid-IR bump, often seen in high-luminosity AGN (e.g. Leipski et al. 2014). Below $5\ \mu\text{m}$, the SEDs are offset by less than 16 per cent, and longwards of $5\ \mu\text{m}$, they are offset by less than 24 per cent.

To develop this comparison further, I also examine the distribution of individual SEDs in the N16 and T15 samples against the distribution of the individual, intrinsic (i.e. with the host component removed) AGN SEDs of the S16 sample (Figs 3–6). Fig. 3 shows that the majority of the N16 SEDs reside within the range of the S16 intrinsic AGN SEDs, except for five sources. Out of those five sources, some have higher $5\ \mu\text{m}$ luminosities, suggesting that the bright far-IR emission might be linked to the elevated mid-IR emission rather than an additional contribution from star formation. To explore this in more detail, I plot the distribution of far-to-mid-IR colour [70-to- $5\ \mu\text{m}$ luminosity ratio; $\nu L_{\nu(70)}/\nu L_{\nu(5)}$] for the N16 sample, in comparison to that of the S16 sample (Fig. 4). Out of the five N16 sources with outlying SEDs, only three (7 per cent of the sample) have far-to-mid-IR colours which extend farther than the tails of the distribution of the S16 sample. It is possible that the different SED slopes of these three sources are due to an additional star formation component. Removing these sources from the N16 sample shifts the far-IR ($70\text{--}150\ \mu\text{m}$) luminosities of the average N16 SED to lower values by 11–15 per cent; nevertheless, the N16 average SED remains consistent with the S16 SED; no data point from the N16 SED is more than 2σ away from the S16 SED.

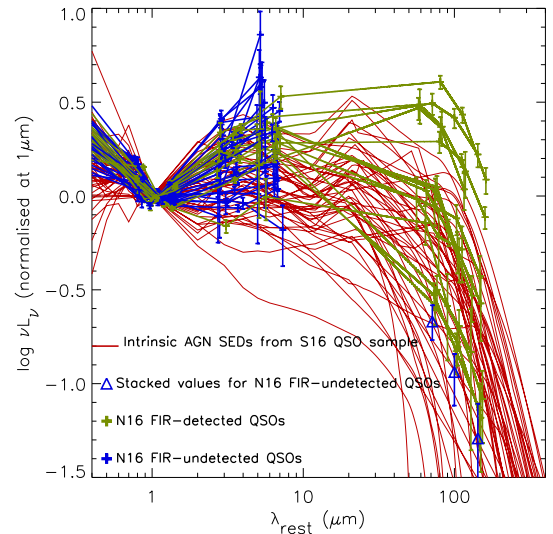


Figure 3. Individual, intrinsic AGN SEDs from S16 shown as red curves, compared with the individual N16 QSO SEDs (blue points for far-IR-undetected sources and green points for far-IR-detected sources)

I perform the same comparison for the T15 sample in Figs 5 and 6, finding no significant differences in the SEDs and distribution in far-to-mid-IR colour of the T15 sample when compared with the S16 sample.

The results presented here indicate that the AGN in the N16 and T15 QSOs could account for the entire broad-band emission from the UV to submm, if indeed the intrinsic AGN emission in these samples is consistent with the one derived in S16 for less powerful, lower redshift QSOs.

3.2 How much star formation is there?

To investigate how much star formation is present in the N16 and T15 QSOs, the S16 intrinsic AGN SED is subtracted from the average QSO T15 SED at 70, 90 and $110\ \mu\text{m}$, and from the average

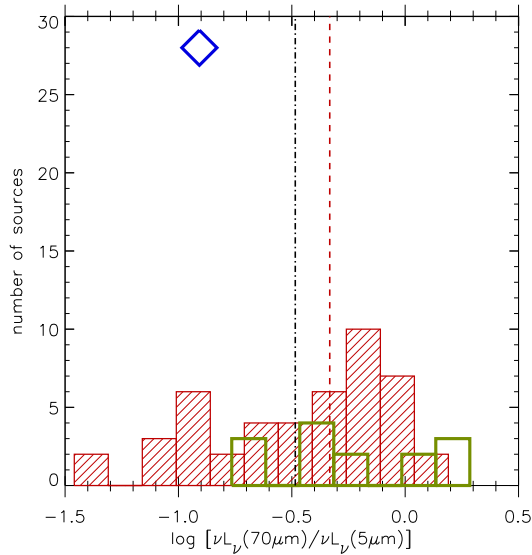


Figure 4. Distribution of the $\log[\nu L_{\nu}(70\ \mu\text{m})/\nu L_{\nu}(5\ \mu\text{m})]$ ratio for the **S16** sample (red hatched histogram) compared to the **N16** sample (blue point for the far-IR-undetected sources using the stacked values and green histogram for the far-IR-detected sources). The dashed red line shows the log of the average $\nu L_{\nu}(70\ \mu\text{m})/\nu L_{\nu}(5\ \mu\text{m})$ ratio for the **S16** sample and the black dot-dashed line shows the log of the weighted average $\nu L_{\nu}(70\ \mu\text{m})/\nu L_{\nu}(5\ \mu\text{m})$ ratio for the **N16** sample (including far-IR-detected and far-IR-undetected sources).

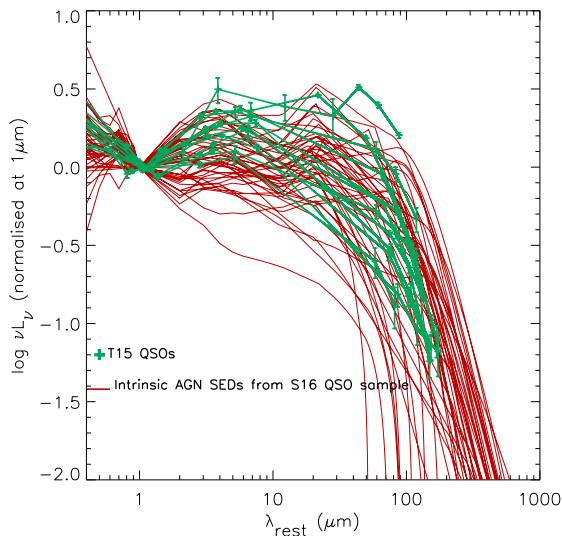


Figure 5. Individual, intrinsic AGN SEDs from **S16** shown as red curves, compared with the individual **T15** QSO SEDs (green points).

N16 SED at 71, 100 and 143 μm , in order to obtain the rest-frame FIR luminosities of the host galaxy SED; the far-IR host galaxy luminosities are shown in Fig. 7 fitted with an M82 SED template (from the GRASIL¹ library; Silva et al. 1998). I find that the total IR luminosity (L_{IR} ; 8–1000 μm) attributed to the host accounts for 0–9 per cent (within 1σ) of the L_{IR} of the **N16** average SED and 0–20 per cent (within 1σ) of the L_{IR} of the **T15** average SED. This suggests that the AGN is responsible for the majority of the total IR emission (over 80 per cent). Using the Kennicutt (1998) relation to

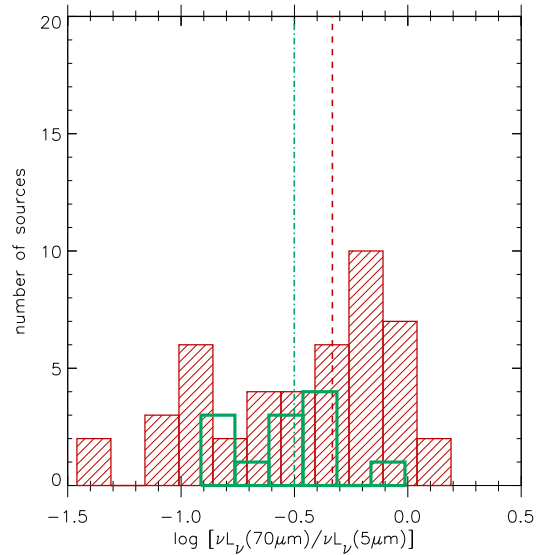


Figure 6. Distribution of the $\log[\nu L_{\nu}(70\ \mu\text{m})/\nu L_{\nu}(5\ \mu\text{m})]$ ratio for the **S16** sample (red hatched histogram) compared to the **T15** sample (green histogram). The log of the average $\nu L_{\nu}(70\ \mu\text{m})/\nu L_{\nu}(5\ \mu\text{m})$ ratio is shown with a red dashed line for the **S16** sample and a green dot-dashed line for the **T15** sample.

convert L_{IR} into an SFR, I find that the upper limit (3σ) on the SFR for the **T15** QSO sample is $3165\ M_{\odot}\ \text{yr}^{-1}$, and for the **N16** sample, it is $643\ M_{\odot}\ \text{yr}^{-1}$. Although this indicates that the SFR could be substantial, a contribution from star formation is not required to account for the IR emission.

3.3 The origin of the far-IR emission in the most luminous QSOs

In Sections 3.1 and 3.2, I showed that a star formation component is not necessary to explain the IR luminosity in the two samples of luminous QSOs studied here and that the emission in the IR can be attributed to dust heated predominantly by the AGN. In the near-/mid-IR, the emission is expected to come from the dust in the torus, heated to near-sublimation temperatures. In the far-IR/submm, there is a contribution from the Rayleigh–Jeans tail of the torus dust emission; however, in **S16** we argued that there is also an additional component of dust which is cooler than that found in the AGN torus, likely dust at kpc scales. We thereafter refer to this as the far-IR-excess component to describe the IR emission from dust not located in the AGN torus but heated by the AGN. As also discussed in **S16**, this component, which is inherently included in the **S16** intrinsic AGN SED, has been missing from previous empirical and modelled SEDs designed to represent the intrinsic AGN emission.

To estimate the mass, size and energy of the far-IR-excess component, one can subtract a torus model from the intrinsic AGN SED. The best model to choose would be one which represents a maximum contribution in the far-IR from the torus, in order to obtain lower limits on the mass, size and energy estimates of the far-IR-excess component. In **S16**, we examined three widely used AGN torus model libraries (torus models from Hönig & Kishimoto 2010, and accretion disc+torus models from Fritz et al. 2006; Siebenmorgen et al. 2015) fitting them to the intrinsic AGN SED; fig. 13 in **S16** shows the ones which are the best fits to the intrinsic AGN SED. Here I chose to use the best-fitting torus model of Fritz

¹ <http://adlibitum.oats.inaf.it/silva/grasil/modlib/modlib.html>

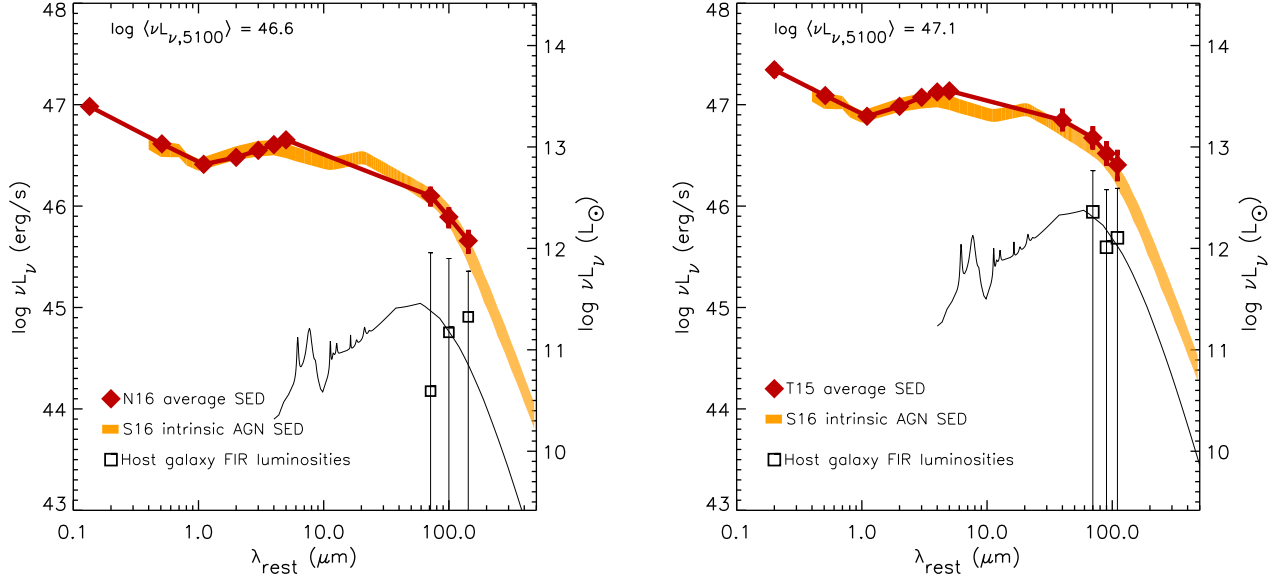


Figure 7. The intrinsic AGN SED from **S16** (shaded orange region where the shading width represents the 1σ bounds) normalized at $1\ \mu\text{m}$ to the average SEDs of the two samples (red diamonds). The **S16** intrinsic AGN SED is subtracted from the average **N16** SED at 71, 100, 143 μm (left panel) and from the average QSO **T15** SED at 70, 90, 110 μm (right panel) in order to obtain the rest-frame FIR luminosities of the host galaxy SED (black open squares). An M82 SED template (from the GRASIL library; Silva et al. 1998) is also shown (black curve) fitted onto the rest-frame FIR host luminosities.

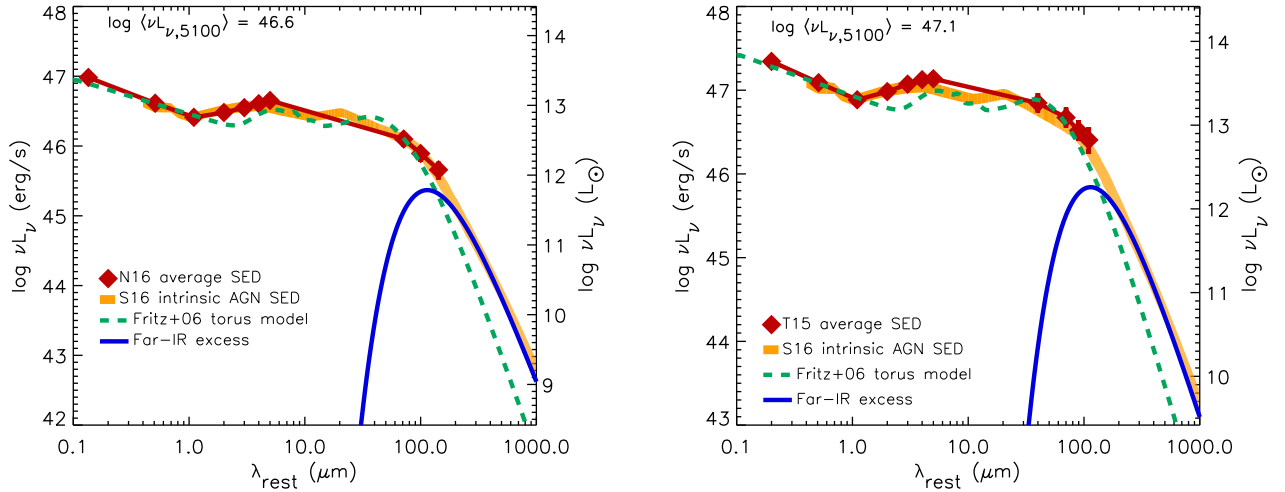


Figure 8. The intrinsic AGN SED from **S16** (shaded orange region where the shading width represents the 1σ bounds) normalized at $1\ \mu\text{m}$ to the average SEDs of the two samples (red diamonds). The best-fitting from the Fritz+06 library (green dashed curve) is subtracted from the intrinsic AGN SED in order to obtain the far-IR-excess component (blue dot-dashed curve). The far-IR-excess component corresponds to the IR emission from dust at kpc scales heated by the AGN.

et al. (2006; see fig. 13 in **S16** and Fig. 8 of this work) as it gives the highest level of far-IR emission for an unobscured, face-on AGN with optical power which matches that of the **S16** intrinsic AGN SED. As stated above, this implies that the mass, size and energy estimates of the far-IR-excess component (see below) should be thought of as lower limits.

I subtract the Fritz et al. (2006) torus model from the **S16** intrinsic AGN SED, normalized to the average SED of each QSO sample (Fig. 8). The subtraction is performed in the 75–1000 μm region only, as at $\sim 75\ \mu\text{m}$ the torus SED crosses the intrinsic AGN SED. The far-IR-excess component can be approximated by a greybody (emissivity $\beta = 1.5$), which peaks at 114 μm (in νL_ν) corresponding to a dust temperature of 23 K. (The equivalent temperature for a blackbody with the same peak is 34 K.) The total amount of energy

it carries is $2.6 \times 10^{45}\ \text{erg s}^{-1}$ ($\pm 1 \times 10^{45}$) for the **N16** sample and $7.7 \times 10^{45}\ \text{erg s}^{-1}$ ($\pm 3 \times 10^{45}$) for the **T15** sample, amounting to 80–87 per cent (within 1σ) of the total QSO power produced longwards of 200 μm . This translates to 5–10 per cent (within 1σ) of the total luminosity of the QSO (integrated in the 0.1–1000 μm range) being emitted in the far-IR.

Its dust mass, M_{dust} , is calculated as follows:

$$M_{\text{dust}} = \frac{f_{\nu, \text{rest}} D_L^2}{B(\nu_{\text{rest}}, T_{\text{dust, rest}}) \kappa_{\text{rest}}}, \quad (1)$$

where D_L is the luminosity distance, $B(\nu_{\text{rest}}, T_{\text{dust, rest}})$ is the blackbody function (in units of flux density), $f_{\nu, \text{rest}} = \frac{f_{\nu, \text{obs}}}{(1+z)}$, $\kappa_{\text{rest}} = \kappa_{850\ \mu\text{m}} \left(\frac{\nu_{\text{rest}}}{\nu_{850\ \mu\text{m}}}\right)^\beta$ and $\kappa_{850\ \mu\text{m}} = 0.0431\ \text{m}^2\ \text{kg}^{-1}$ taken from Li &

Table 1. Properties of the far-IR-excess component for the QSO samples examined in this work. This component can be approximated by a greybody of peak wavelength $114 \mu\text{m}$ (in νL_ν), emissivity $\beta = 1.5$ and dust temperature 23 K . Its emission relates to dust at kpc scales heated by the AGN and makes up 5–10 per cent of the total AGN luminosity (integrated in the $0.1\text{--}1000 \mu\text{m}$ range) and 80–87 per cent of the total power produced longwards of $200 \mu\text{m}$.

QSO sample	$\log L_{\text{dust}}$ (erg s^{-1})	$\log M_{\text{dust}}$ (M_\odot)	R_{dust} (kpc)
N16	45.4	8	>1.2
T16	45.9	8.5	>2.2

Draine (2001). Here, I take ν_{rest} as the rest-frame frequency equivalent to $850 \mu\text{m}$ (observed), $\beta = 1.5$ and $T_{\text{dust, rest}} = 34 \text{ K}$. $f_{\nu, \text{obs}}$ at $850 \mu\text{m}$ is computed from the SED of the far-IR-excess component, using $z_{\text{mean}} = 2.7$ for the N16 QSOs and $z_{\text{mean}} = 2.8$ for the T15 QSOs. The dust mass calculated for the N16 sample is $1.1 \times 10^8 M_\odot$, and for the T15 sample, it is $3.2 \times 10^8 M_\odot$.

Finally, to estimate the extent of the dust region which corresponds to the far-IR-excess emission, I use the Stefan–Boltzmann law for a greybody, $P = A\epsilon_{\text{GB}}\sigma T^4$. In this case, P is the power carried by the far-IR-excess component (as calculated above), A is the area of the emitting greybody ($= 4\pi r^2$, where r is the radius), σ is the Stefan–Boltzmann constant, ϵ_{GB} is the emissivity of the greybody and T is the temperature of the far-IR-excess component. To compute ϵ_{GB} , I take the ratio of integrated greybody function (23 K ; $\beta = 1.5$) to the integrated blackbody function (34 K ; normalized to the far-IR-excess component peak) to be equal to the ratio of the emissivity of the greybody (ϵ_{GB}) to the emissivity of the blackbody ($\epsilon_{\text{BB}} = 1$); i.e. $\frac{\text{GB}}{\text{BB}} = \epsilon_{\text{GB}}$ (see also Greve et al. 2012 for an equivalent method). I find $\epsilon_{\text{GB}} = 0.87$ and arrive at a radius, r , of 1.2 kpc for the N16 sample and 2.2 kpc for the T15 sample. Note that this is the minimum radius of the extended dust region heated by the AGN, assuming that the dust filling factor is 100 per cent. In practice, the size of the dust region illuminated by the AGN will likely extend to several kpc, as the dust filling factor is much less than 100 per cent.

The properties of the far-IR-excess component in the two QSO samples are presented in Table 1.

4 DISCUSSION AND CONCLUSIONS

I find that, over the entire UV–submm wavelength range, the average SED shape of the most luminous unobscured QSOs at $2 < z < 3.5$ matches that of the average intrinsic AGN SED derived in S16 from a set of lower redshift ($z < 0.18$) QSOs, two to three orders of magnitude less luminous in the optical. Indeed, it has been shown that the X-ray-to-mid-IR SEDs and spectra of QSOs do not evolve as a function of redshift or AGN luminosity (e.g. Wilkes et al. 1994; Mathur, Wilkes & Ghosh 2002; Grupe et al. 2006; Hao et al. 2014), so one might expect that their far-IR SEDs are also unchanged.

On the basis of the assumption that the intrinsic AGN emission as a function of wavelength is broadly independent of AGN luminosity [for $\nu L_{\nu, 5100}$ or $L_{\text{X}(2\text{--}10\text{keV})} > 10^{43.5} \text{ erg s}^{-1}$ AGN] and redshift (at least up to $z \sim 3.5$), my results indicate that, on average, the far-IR/submm emission in the most luminous QSOs at the tail of the $2 < z < 4$ optical luminosity function (Richards et al. 2006) is primarily produced by the AGN. This implies that for such systems, the emission in the *Herschel* bands and longer wavelengths such as those probed by SCUBA-2 at $850 \mu\text{m}$ would be AGN dominated; thus, wide-area *Herschel* and SCUBA-2 surveys will contain a population of QSOs which are primarily powered by AGN. More-

over, the SFRs of such systems cannot be determined with X-ray to submm broad-band photometry, and other means such as IR spectral lines will need to be used. Note that this does not mean that the host galaxies of luminous QSOs do not have star formation, perhaps even a considerable amount: I calculate a 3σ upper limit on the SFR of 3165 and $643 M_\odot \text{ yr}^{-1}$ for the two QSO samples studied here. It simply means that the contribution from star formation is not detected in the broad-band SED as it is energetically less prominent than the AGN power at all wavelengths. This conclusion is in disagreement with the work of N16. N16 use an AGN torus template to decompose their QSO SEDs into an AGN torus component and a star-forming component. The torus template used by N16 has a steeper far-IR slope than the S16 AGN SED, falling by about 0.5 dex between 50 and $70 \mu\text{m}$, compared to a 0.1 dex change in the S16 AGN SED. This implies that a smaller fraction of the far-IR emission is attributed to the AGN in the work of N16, and indeed, they find that star formation is a significant contributor to emission in the *Herschel* bands. In S16, however, we argued that using torus templates in SED decomposition can significantly underestimate the AGN power in the far-IR, as they often lack an extended dust component, which would, in turn, boost the contribution required from star formation. Other works which use SED decomposition to separate the AGN and star formation contributions also find that QSOs have IR luminosities systematically larger than the IR luminosity produced by a torus component (e.g. Leipski et al. 2014; Drouart et al. 2016; Gruppioni et al. 2016; Podigachoski et al. 2016). Although traditionally this has been assigned to star formation, here I argue that a significant fraction, and in some cases all, of this excess IR luminosity can be attributed to AGN-heated dust at kpc scales.

Using a bolometric correction factor $f = 4$, where $L_{\text{AGN, bol}} = f \times \nu L_{\nu, 5100}$, and an efficiency of $\eta = 0.1$ to convert AGN luminosity into black hole accretion rate (BHAR) as in N16, I calculate a 3σ upper limit on the SFR/BHAR ratio of 23 for the N16 sample and 36 for the T15 sample. However, note that higher values of f have also been reported ($f = 5\text{--}13$; e.g. Elvis et al. 1994; Kaspi, Brandt & Schneider 2000; Netzer 2003; Marconi et al. 2004; Netzer & Trakhtenbrot 2007), suggesting that the SFR/BHAR upper limit could be even lower. A value of SFR/BHAR ~ 500 corresponds to the black hole–galaxy bulge mass relation in the local Universe, i.e. black holes growing in tandem with their hosts, and SFR/BHAR = 142 corresponds to $L_{\text{SF}} \sim L_{\text{AGN}}$ (e.g. Alexander & Hickox 2012; N16). N16 report larger values of SFR/BHAR than the upper limit I calculate here, particularly for their far-IR-detected QSOs, as they assume a greater level of contribution from star formation in the far-IR. They also find that some sources in their sample are very close to the $L_{\text{SF}} \sim L_{\text{AGN}}$ regime. In contrast, my findings suggest that the most luminous QSOs at $2 < z < 4$ have L_{AGN} considerably larger than L_{SF} and are hence AGN-dominated. Using hydrodynamical simulations of galaxy mergers, Volonteri et al. (2015) propose that such AGN-dominated galaxies are likely to be either in the merger or in the remnant phase, with a BHAR at a given SFR about 20 times higher than for star formation dominated galaxies.

I find that at least 5–10 per cent of the bolometric AGN luminosity is absorbed by dust beyond the torus, at kpc scales, and re-emitted in the far-IR/submm, accounting for the major fraction of the global emission longwards of $200 \mu\text{m}$. This is consistent with Baron et al. (2016), who find that the typical optical–UV continuum slopes of optically unobscured QSOs are reddened by dust along the line of sight, corresponding to a total luminosity emitted in the far-IR of the order of 15 per cent of the AGN bolometric luminosity. I calculate that the extent of the dust region illuminated by the AGN

in the most powerful QSOs is at least a few kpc, comparable to those reported for submm galaxies and other high-redshift QSOs – studies with the Plateau de Bure Interferometer, the SMA and ALMA (e.g. Riechers et al. 2009; Bothwell et al. 2010; Carilli et al. 2010; Younger et al. 2010; Hodge et al. 2013; Wang et al. 2013; Simpson et al. 2015) measure the dust full width at half-maximum to be 1–10 kpc, with a mean/median within the lower half of this range. Moreover, the implied dust masses of the order of $10^8 M_{\odot}$ are comparable to those of star-forming IR-luminous galaxies (e.g. Santini et al. 2010, 2014; Dunne et al. 2011) and consistent with those calculated for other high-redshift QSO samples (e.g. Bertoldi et al. 2003; Beelen et al. 2006; Wang et al. 2008, 2011).

I find that the relative power carried by the far-IR/submm component is independent of AGN luminosity (for $\nu L_{\nu, 5100}$ or $L_{X(2-10\text{keV})} > 10^{43.5} \text{ erg s}^{-1}$ AGN), implying a constant far-IR dust temperature. According to the Stefan–Boltzmann law, this suggests that the radius of the corresponding dust region must scale with $\sqrt{L_{\text{AGN}}}$. For this dust to be directly heated by the AGN, it is likely to be within the ionization cone of the AGN; indeed, there is evidence for the presence of dust in the narrow-line regions (NLRs) of AGN from spectropolarimetry data (e.g. Goodrich 1989, 1992; Vernet et al. 2001; Smith et al. 2004). Furthermore, my estimates for the size of the dust region and its dependence on the AGN luminosity are consistent with reported values of <20 kpc for the extent of the NLR (e.g. Hainline et al. 2013, 2014; Liu et al. 2013) and its suggested scaling with $\sqrt{L_{\text{AGN}}}$ (e.g. Bennert et al. 2002; Hainline et al. 2013).

ACKNOWLEDGEMENTS

This work was supported by the UK Science and Technology Facilities Council.

REFERENCES

- Alam S. et al., 2015, ApJS, 219, 12
 Alexander D. M., Hickox R. C., 2012, New Astron. Rev., 56, 93
 Baron D., Stern J., Poznanski D., Netzer H., 2016, ApJ, 832, 8
 Beelen A., Cox P., Benford D. J., Dowell C. D., Kovács A., Bertoldi F., Omont A., Carilli C. L., 2006, ApJ, 642, 694
 Bennert N., Falcke H., Schulz H., Wilson A. S., Wills B. J., 2002, ApJ, 574, L105
 Bertoldi F., Carilli C. L., Cox P., Fan X., Strauss M. A., Beelen A., Omont A., Zylka R., 2003, A&A, 406, L55
 Bothwell M. S. et al., 2010, MNRAS, 405, 219
 Boyle B. J., Terlevich R. J., 1998, MNRAS, 293, L49
 Bower R. G., Benson A. J., Malbon R., Helly J. C., Frenk C. S., Baugh C. M., Cole S., Lacey C. G., 2006, MNRAS, 370, 645
 Carilli C. L. et al., 2010, ApJ, 714, 1407
 Colless M. et al., 2001, MNRAS, 328, 1039
 Croton D. J. et al., 2006, MNRAS, 365, 11
 De Rosa G. et al., 2011, ApJ, 739, 56
 Delvecchio I. et al., 2015, MNRAS, 449, 373
 Drouart G. et al., 2014, A&A, 566, A53
 Drouart G., Rocca-Volmerange B., De Breuck C., Fioc M., Lehnert M., Seymour N., Stern D., Vernet J., 2016, A&A, 593, A109
 Dunne L. et al., 2011, MNRAS, 417, 1510
 Elvis M. et al., 1994, ApJS, 95, 1
 Ferrarese L., Merritt D., 2000, ApJ, 539, L9
 Feruglio C. et al., 2014, A&A, 565, A91
 Fritz J., Franceschini A., Hatziminaoglou E., 2006, MNRAS, 366, 767
 Goodrich R. W., 1989, ApJ, 340, 190
 Goodrich R. W., 1992, ApJ, 399, 50
 Greenstein J. L., Matthews T. A., 1963, AJ, 68, 279
 Greve T. R. et al., 2012, ApJ, 756, 101
 Grupe D., Mathur S., Wilkes B., Osmer P., 2006, AJ, 131, 55
 Gruppioni C. et al., 2016, MNRAS, 458, 4297
 Hainline K. N., Hickox R., Greene J. E., Myers A. D., Zakamska N. L., 2013, ApJ, 774, 145
 Hainline K. N., Hickox R. C., Greene J. E., Myers A. D., Zakamska N. L., Liu G., Liu X., 2014, ApJ, 787, 65
 Hao H. et al., 2014, MNRAS, 438, 1288
 Hirschmann M., Dolag K., Saro A., Bachmann L., Borgani S., Burkert A., 2014, MNRAS, 442, 2304
 Hodge J. A. et al., 2013, ApJ, 768, 91
 Höning S. F., Kishimoto M., 2010, A&A, 523, A27
 Jones D. H. et al., 2009, MNRAS, 399, 683
 Kaspi S., Brandt W. N., Schneider D. P., 2000, AJ, 119, 2031
 Kennicutt R. C., Evans N. J., 2012, ARA&A, 50, 531
 Khandai N., Feng Y., DeGraf C., Di Matteo T., Croft R. A. C., 2012, MNRAS, 423, 2397
 Lawrence A. et al., 2007, MNRAS, 379, 1599
 Leipski C. et al., 2014, ApJ, 785, 154
 Li A., Draine B. T., 2001, ApJ, 554, 778
 Liu G., Zakamska N. L., Greene J. E., Nesvadba N. P. H., Liu X., 2013, MNRAS, 436, 2576
 Mainieri V. et al., 2011, A&A, 535, A80
 Magorrian J. et al., 1998, AJ, 115, 2285
 Marconi A., Risaliti G., Gilli R., Hunt L. K., Maiolino R., Salvati M., 2004, MNRAS, 351, 169
 Mathur S., Wilkes B. J., Ghosh H., 2002, ApJ, 570, L5
 Melia F., 2014, AJ, 147, 120
 Merloni A., Rudnick G., Di Matteo T., 2004, MNRAS, 354, L37
 Mullaney J. R. et al., 2015, MNRAS, 453, L83
 Netzer H., 2003, ApJ, 583, L5
 Netzer H., Trakhtenbrot B., 2007, ApJ, 654, 754
 Netzer H., Mor R., Trakhtenbrot B., Shemmer O., Lira P., 2014, ApJ, 791, 34
 Netzer H., Lani C., Nordon R., Trakhtenbrot B., Lira P., Shemmer O., 2016, ApJ, 819, 123 (N16)
 Osterbrock D. E., Ferland G. J., 2006, Astrophysics of Gaseous Nebulae and Active Galactic Nuclei, 2nd edn. University Science Books, Mill Valley, CA
 Podgachoski P. et al., 2015, A&A, 575, A80
 Podgachoski P., Rocca-Volmerange B., Barthel P., Drouart G., Fioc M., 2016, MNRAS, 462, 4183
 Rawlings J. I. et al., 2013, MNRAS, 429, 744
 Richards G. T. et al., 2006, AJ, 131, 2766
 Riechers D. A. et al., 2009, ApJ, 703, 1338
 Rodríguez-Ardila A., Mazzalay X., 2006, MNRAS, 367, 57
 Rosario D. J. et al., 2013, A&A, 560, A72
 Rovilos E. et al., 2012, A&A, 546, A58
 Santini P. et al., 2010, A&A, 518, L154
 Santini P. et al., 2014, A&A, 562, A30
 Schmidt M., 1963, Nature, 197, 1040
 Silva L., Granato G. L., Bressan A., Danese L., 1998, ApJ, 509, 103
 Silverman J. D. et al., 2008, ApJ, 679, 118
 Simpson J. M. et al., 2015, ApJ, 799, 81
 Skrutskie M. F. et al., 2006, AJ, 131, 1163
 Smith J. E., Robinson A., Alexander D. M., Young S., Axon D. J., Corbett E. A., 2004, MNRAS, 350, 140
 Symeonidis M. et al., 2011, MNRAS, 417, 2239
 Symeonidis M. et al., 2014, MNRAS, 443, 3728
 Symeonidis M., Giblin B. M., Page M. J., Pearson C., Bendo G., Seymour N., Oliver S. J., 2016, MNRAS, 459, 257 (S16)
 Tsai C.-W. et al., 2015, ApJ, 805, 90 (T15)
 Vernet J., Fosbury R. A. E., Villar-Martín M., Cohen M. H., Cimatti A., di Serego Alighieri S., Goodrich R. W., 2001, A&A, 366, 7
 Volonteri M., 2012, Science, 337, 544

Volonteri M., Capelo P. R., Netzer H., Bellovary J., Dotti M., Governato F.,
2015, MNRAS, 452, L6
Wang R. et al., 2008, AJ, 135, 1201
Wang R. et al., 2011, AJ, 142, 101
Wang R. et al., 2013, ApJ, 773, 44
Wilkes B. J., Tananbaum H., Worrall D. M., Avni Y., Oey M. S., Flanagan
J., 1994, ApJS, 92, 53

Willott C. J. et al., 2010a, AJ, 140, 546
Willott C. J. et al., 2010b, AJ, 139, 906
Wu X.-B. et al., 2015, Nature, 518, 512
Younger J. D. et al., 2010, MNRAS, 407, 1268

This paper has been typeset from a $\text{\TeX}/\text{\LaTeX}$ file prepared by the author.